Large-scale dynamic triggering of shallow slow slip enhanced by overlying sedimentary wedge

Laura M. Wallace[1,2]*, Yoshihiro Kaneko[1], Sigrún Hreinsdóttir[1], Ian Hamling[1], Zhigang Peng[3], Noel Bartlow[4], Elisabetta D'Anastasio[1] and Bill Fry[1]

Slow slip events have become recognized in the last decade as an important mode of fault slip, and are most widely observed at subduction zones. Many episodes of tectonic tremor (related to slow slip) have been triggered by distant earthquakes due to dynamic-stress changes from passing seismic waves. However, there are few clear examples of large, geodetically detected slow slip events triggered by distant earthquakes. Here we use analyses of seismic and geodetic data to show that the magnitude 7.8 Kaikōura earthquake in New Zealand in 2016 triggered a large slow slip event between 250 and 600 km away. The slow slip was shallow, at less than 15 km deep, and spanned more than 15,000 km^2 of the central and northern Hikurangi subduction margin. The slow slip initiated immediately after the earthquake, lasted one to two weeks and was accompanied by a swarm of seismicity. We show that changes in dynamic stress in the slow slip source area ranged from 100 to 600 kPa—approximately 1,000 times greater than the static-stress changes of 0.2 to 0.7 kPa. We therefore propose that the slow slip event was triggered by dynamic-stress changes caused by passing seismic waves. Furthermore, the dynamic-stress changes were greatest on the shallow subduction interface, at less than 10 km depth, in a region overlain by a sedimentary wedge that acts as a waveguide, trapping seismic energy and probably promoting triggering of slip. This suggests that shallow slow slip events are more easily triggered by dynamic-stress changes compared with deep events.

Despite widespread observations of slow slip events (SSEs) at subduction zones and other types of environment around the globe[1–4], the relationship between SSEs and seismic slip is still not well understood. Many observations indicate that SSEs can trigger damaging seismic events[5–9]. There are also abundant observations of seismic events triggering slow slip and related seismic phenomena. These include deep tectonic tremor episodes triggered by dynamic-stress changes from passing seismic waves from regional or distant earthquakes[3,10–12], and observations of earthquakes triggering nearby (<50 km), geodetically detectable SSEs due to either dynamic- or static-stress changes[13,14]. However, there are very few (if any) clear-cut examples of regional or distant seismic events dynamically triggering large-scale, geodetically detectable SSEs. The primary examples of distant or regional triggering of geodetically detected subduction-zone SSEs include a possible small SSE observed in strainmeter data in southwest Japan triggered by a distant event near Tonga in 2009[15], a long-term (~6 months) SSE in Mexico postulated to be triggered by the 2010 Maule earthquake[16], small triggered SSEs (~2–4 cm slip) near the trench at the Nankai Trough[17], and recurrent SSEs in Boso Peninsula brought forward in time (although not immediately) by the 2011 Tohoku-Oki earthquake[18]. Some cases were accompanied by tremor or low-frequency earthquakes[16,17], or earthquake swarms[18]. Dynamically triggered SSEs from distant earthquakes have also been documented on the strike-slip San Andreas system from creepmeter data[19], and tremor and low-frequency earthquakes[20]. Slow onset and longer duration (months) of some large, geodetically detectable subduction SSEs[16] can make it difficult to establish a dynamic triggering origin. Whether or not dynamic triggering of SSEs can occur over a large region (for example, many thousands of square kilometres) has implications for the strength of large portions of subduction plate boundaries.

Slow slip following the Kaikōura earthquake

New Zealand straddles the boundary zone between the Australian and Pacific plates (Fig. 1). Just after midnight on 14 November 2016 (New Zealand local time), the $M7.8$ Kaikōura earthquake ruptured a complex sequence of at least a dozen crustal strike-slip and reverse faults over a ~150 km length of the plate boundary in the northeastern South Island[21,22]. The earthquake primarily involved right-lateral strike-slip and some reverse faulting within the Marlborough fault system and northern Canterbury area[21]. It is also likely that the earthquake involved slip on the far southern Hikurangi subduction interface beneath the northern South Island[21].

Immediately following the earthquake, continuous GPS (cGPS) sites operated by GeoNet (www.geonet.org.nz) along the North Island's east coast (above the Hikurangi subduction zone) detected several to 30 mm of eastward motion over the one- to two-week period after the earthquake (Figs 1 and 2). Some cGPS sites at the northern Hikurangi margin underwent 5–10 mm of eastward displacement within 5 h after the earthquake (Fig. 2). These cGPS sites were 250–600 km from the $M7.8$ earthquake, in a region coseismically displaced 1–4 mm northwards by the $M7.8$ earthquake (Supplementary Fig. 1). Such large eastward motion following the earthquake is at odds with Kaikōura $M7.8$ coseismic and postseismic signals expected at these sites, and is instead consistent with initiation of a large SSE along the offshore Hikurangi subduction zone (Fig. 1). Displacement patterns are similar to those observed in previous SSEs in that region[23].

[1]GNS Science, Lower Hutt 5011, New Zealand. [2]University of Texas Institute for Geophysics, Austin, Texas 78758, USA. [3]School of Earth and Atmospheric Science, Georgia Tech, Atlanta, Georgia 30332, USA. [4]Department of Geological Sciences, University of Missouri, Columbia, Missouri 65211, USA. *e-mail: l.wallace@gns.cri.nz
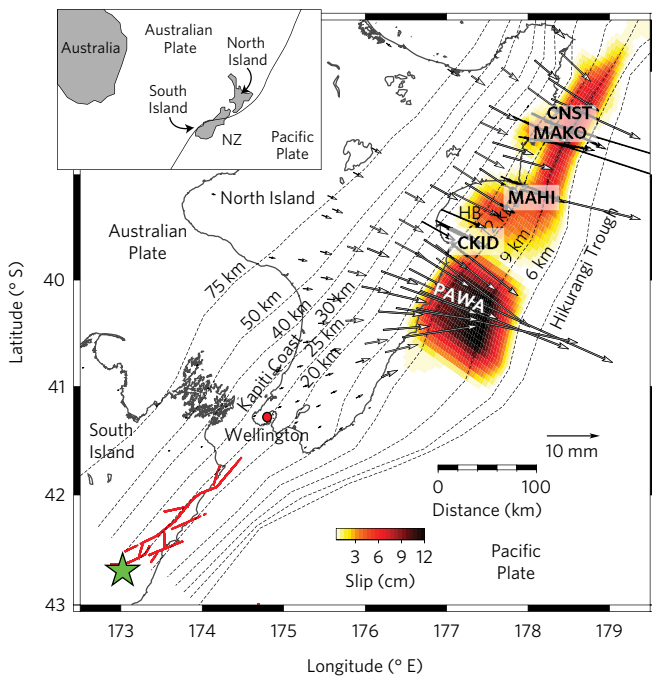
Figure 1 | Total slip on the shallow Hikurangi subduction interface following the 2016 Kaikōura M7.8 earthquake. Slow slip on the Hikurangi subduction interface (colours, see scale in cm) following the 14 November 2016 M7.8 earthquake (green star). The arrows show horizontal displacement of cGPS sites during the SSE based on the best-fitting model (see Supplementary Fig. 4a,b for cGPS time series and model fits). The red lines show the surface traces of faults that ruptured in the earthquake[21]. The black dashed contours represent the Hikurangi subduction interface, with depths in kilometres below sea level. HB, Hawke Bay. The southern Hawkes Bay region is the area to the south of Hawke Bay. cGPS site locations labelled for those in Fig. 2.

Slow slip event evolution and relationship to seismicity

We invert cGPS time series for slip on the Hikurangi subduction zone using a time-dependent, nonlinear inversion code, TDEFN-ODE[24] (see Methods), using the most recent Hikurangi subduction geometry[25] to define the interface in our model. Daily cGPS time series are from GeoNet (www.geonet.org.nz), and we also include time series of 8-h GPS solutions (some are shown in Fig. 2b) from many of the sites on the east coast. Best-fitting slip models require SSE slip on the shallow subduction interface (<15 km deep) off-shore most of the east coast of the North Island during the ten-day period following the M7.8 Kaikōura earthquake (Figs 1 and 3). We confirm these results with a different time-dependent inversion code, the Network Inversion Filter[26,27] (Supplementary Fig. 2 and Methods). SSE displacements began at the northern Hikurangi margin immediately following the M7.8 earthquake, while sites at the central Hikurangi margin showed large displacements within 2–3 days of the earthquake (sites PAWA and PORA) (Fig. 2). This suggests two possible scenarios: the SSE initiated at the northern Hikurangi margin and migrated south; or the SSE initiated in both locations nearly simultaneously, but central Hikurangi margin slip began near the trench and migrated down-dip, producing visible displacements at shore-based GPS sites a couple of days after the earthquake. Without seafloor geodetic data, it is difficult to distinguish between these two scenarios. However, the lack of seismicity offshore the southern patch of SSE slip during the first 5–6 days after the earthquake (Fig. 3) suggests that the second scenario may be more likely, as SSEs in this portion of the Hikurangi margin tend to excite microseismicity[28,29]. The cumulative moment released in the SSE is $M_w 7.1$, assuming a shear modulus of 30 GPa.

Since the GeoNet cGPS network began operating in 2002, we have observed numerous SSEs on the offshore northern and central Hikurangi subduction zone. These offshore SSEs generally occur at <15 km depth, are short in duration (<2–3 weeks), and typically involve 1–3 cm of eastward movement of cGPS sites on the east coast[23,28], similar to the SSE following the Kaikoura earthquake. However, previous shallow Hikurangi SSEs have typically ruptured smaller portions of the interface, separated in space and time[23,28,29]. This is the first time that near-simultaneous rupture of the entire central and north Hikurangi margin shallow slow slip region has been observed, with an SSE rupture length of $\sim$300 km. The large regional extent of the SSE rupture, and initiation immediately following the Kaikōura M7.8 earthquake, suggests that the earthquake triggered the SSE. We note that deeper (30–40 km) slow slip and afterslip also follows the Kaikōura earthquake at the southern Hikurangi subduction margin (http://www.geonet.org.nz/news/18hVgzaAdgaGC6CcWmwmU6). Because these southern Hikurangi events are still ongoing (and new data are being acquired to better understand these), we limit this study to long-distance ($>$250 km) triggering of east coast SSEs.

The largest SSE slip is observed offshore the southern Hawkes Bay region ($>$10 cm), and was accompanied by abundant seismicity (Fig. 3), with numerous events in the $M_w 2.0$–5.0 range, and up to $M_w 6.0$ (www.geonet.org.nz). Focal mechanisms from larger events in the swarm are consistent with a subduction interface origin[30]. We also detect many repeating earthquakes co-located in this region[5,31], probably driven by the ongoing SSE (Fig. 3). Two previous SSEs have been observed in this area, in 2006 and 2011[23,28], suggesting an approximately five-year recurrence interval between SSEs in southern Hawkes Bay, and were similarly accompanied by elevated seismicity rates[28,29]. On the basis of the previous five-yearly recurrence patterns of past SSEs in southern Hawkes Bay, this region was already late in its SSE cycle, and was more susceptible to triggering by the M7.8 earthquake. In contrast, the northern Hikurangi margin (where SSEs occur every 1–2 years) had already undergone a few SSE episodes earlier in 2016 (Supplementary Fig. 3), and was not clearly due for another SSE. This suggests that the northern Hikurangi margin SSEs may be highly susceptible to small stress perturbations independent of where it is in the SSE cycle.

Large slow slip triggered by dynamic-stress changes

The physical conditions and mechanisms leading to SSE occurrence are still under debate, although most agree that SSEs occur on faults with low effective stress, due to the presence of high pore fluid pressures[32,33]. Such physical conditions make SSE regions sensitive to small stress perturbations (tens of kilopascals) from local and regional earthquakes, both in terms of static-stress[13] and dynamic-stress[3,16,20] changes, and tidal perturbations[34,35]. To determine whether large, widespread SSE triggering off the North Island's east coast is due to dynamic- or static-stress changes induced by the Kaikōura earthquake, we undertake modelling of these stress changes on the subduction interface fault.

We calculate the static-stress change on the subduction interface due to the coseismic slip distribution in the Kaikōura earthquake (Fig. 4a inset, and 4b) using a model that includes some slip on the subduction interface beneath the northern South Island[21]. We calculate Coulomb stress changes[36] on the Hikurangi interface assuming long-term slip directions on the subduction interface[37], and an effective coefficient of friction[38] of 0.1. Static-stress increases of $>$0.5 MPa are predicted on the far southern Hikurangi interface beneath the northeast South Island, while a large static-stress decrease is predicted east of the Kaikōura M7.8 rupture area (Fig. 4a inset). In the east coast shallow SSE region, static-stress changes are exceedingly small (0.2–0.7 kPa; Fig. 4b), much smaller than stress changes exerted by tidal loading calculated for offshore thrust plate boundaries, which are typically on the order of 10 kPa or
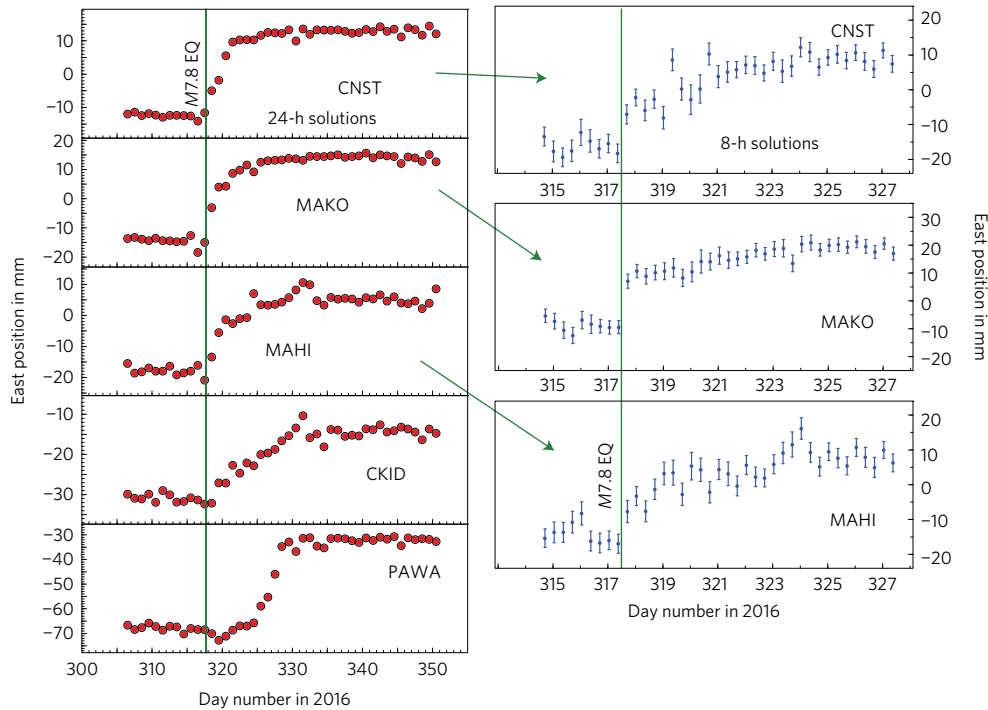
Figure 2 | Continuous GPS time series showing east coast slow slip following the Kaikōura earthquake. The east component of cGPS site positions for representative sites on the east coast; the green line on each shows the time of the earthquake. The time series on the left (in red) are positions for each 24-h period, available at www.geonet.org.nz. Note the onset of SSE slip at cGPS sites further south (PAWA) a few days after the earthquake. The time series on the right (in blue) show positions for each 8-h period at a subset of sites at the northern Hikurangi margin north, where SSE displacement initiated immediately. Locations of sites shown on Fig. 1.
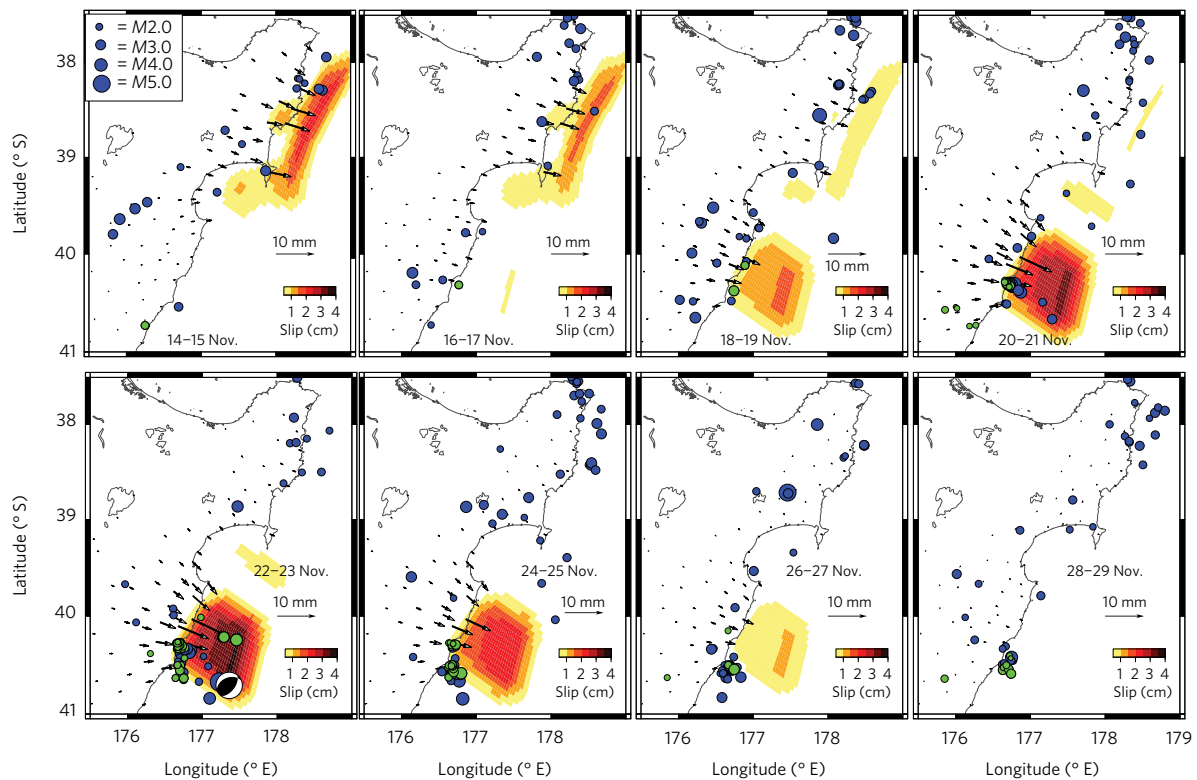
Figure 3 | Evolution of shallow slow slip on the Hikurangi subduction zone during the days following the Kaikōura earthquake. Time-dependent slip inversion results from TDEFNODE (see Methods) during the time following the Kaikōura M7.8 earthquake. Slip amounts on the interface are shown in centimetres (yellow to red colours), and horizontal displacements for the cGPS sites from the best-fitting model are shown as arrows (with scale). Fits for this model to the cGPS time series are in Supplementary Fig. 4. The blue circles are earthquakes from the GeoNet catalogue for each time slice, and the green circles are repeating earthquakes determined from template matching (see Methods). The focal mechanism on the fifth panel is for the M_w 6.0 thrust event on 22 November 2016 from www.geonet.org.nz.
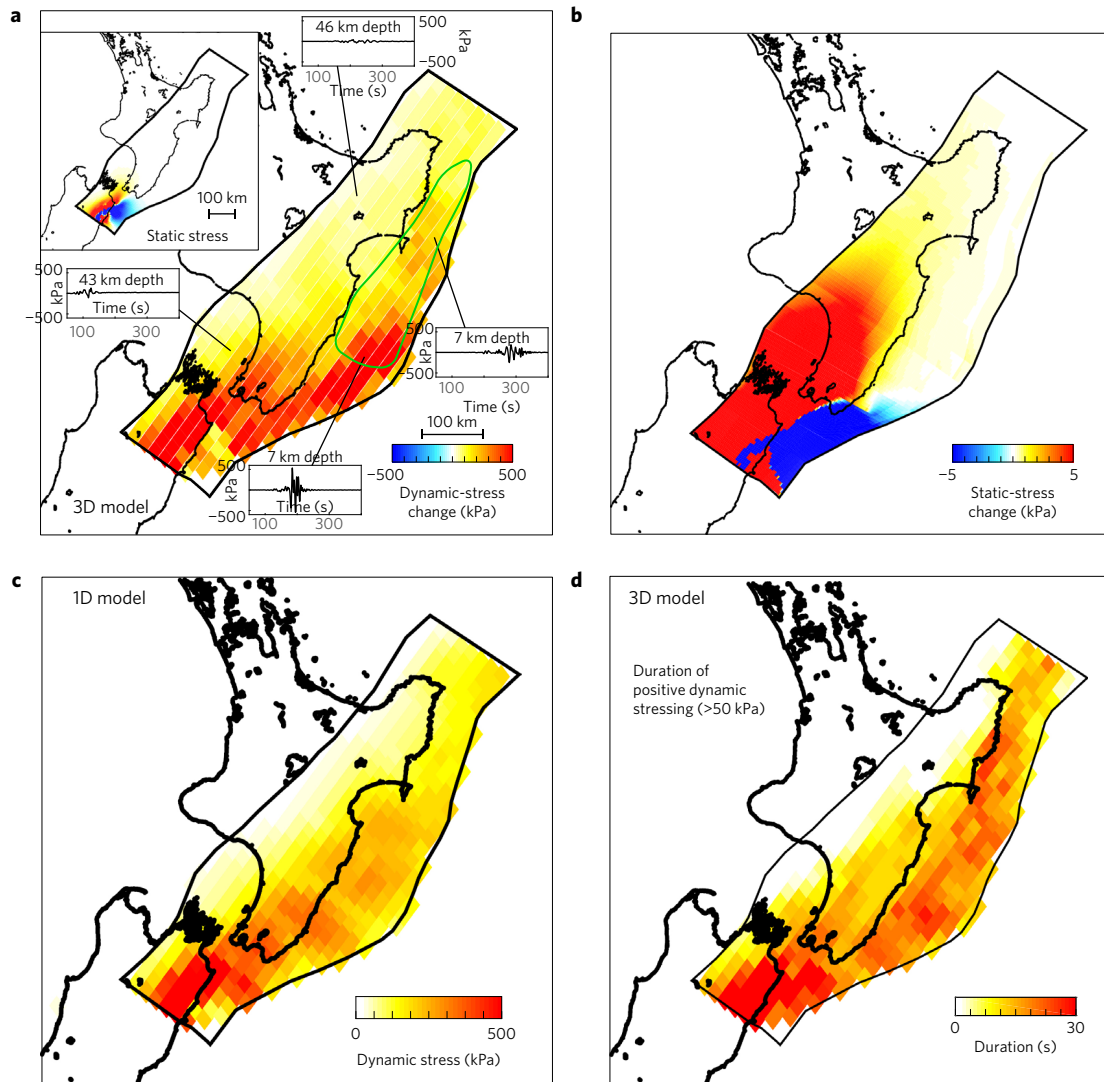
Figure 4 | Stress changes on the Hikurangi interface induced by the Kaikōura earthquake. a,b, Changes in dynamic stress (using a 3D velocity model) (**a**) and static stress (**b**). Dynamic-stress change is the maximum during the time period considered. The green contour outlines triggered SSE. The inset in the upper left shows the static-stress change at the same colour scale as the dynamic-stress change. Dynamic- and static-stress changes assume an effective coefficient of friction = 0.1. The graphs in **a** show stress change with time during the earthquake predicted by our rupture model at specified points on the subduction interface (y axis is stress change in kPa). Note the different colour scales for the stress change in **a** and **b**. **c**, Peak dynamic-stress changes using a 1D, layered velocity model. **d**, Duration of positive dynamic stressing >50 kPa for the 3D case (1D model durations in Supplementary Fig. 9).

more[39]. This makes a static-stress triggering origin for the east coast SSE unlikely.

Dynamic-stress changes due to passing seismic waves can be on the order of tens to hundreds of kilopascals (ref. 40), even at great distances from an earthquake[41]. Using a kinematic source model of the $M7.8$ Kaikōura earthquake derived from the above-mentioned slip model and local strong-motion and high-rate GPS waveforms (Methods), we compute the corresponding time-dependent Coulomb stress changes on the Hikurangi subduction interface assuming an effective coefficient of friction of 0.1. The pattern of maximum dynamic-stress changes on the subduction interface depends on four primary factors: the proximity to the source, interface depth, local three-dimensional (3D) velocity structure, and earthquake source processes including rupture directivity (Fig. 4a). To first order, the regions of large dynamic-stress changes are controlled by northeastward rupture directivity during the earthquake. At a large (>200 km) distance from the source, the amplitude of surface waves, which is the largest signal in the velocity waveforms, sharply decays with depth. Since the

amplitude of velocity waveforms is approximately proportional to that of stress changes, shallower interface regions become more susceptible to dynamic triggering of slip events.

Most remarkably, a basin effect combined with rupture directivity is observed on the shallow interface overlain by the low-velocity ($V_s < 2,500\ \mathrm{m\,s^{-1}}$) sedimentary wedge of the outer forearc (Supplementary Fig. 7), trapping the seismic energy and amplifying dynamic-stress changes there. Offshore the North Island's east coast, at distances of more than 250 km from the Kaikōura earthquake, these dynamic-stress changes are 100 to 600 kPa (Fig. 4a), approximately 1,000 times larger than the expected static-stress changes (Fig. 4). In contrast, dynamic-stress changes predicted for the deeper portions of the interface <100 km from the Kaikōura earthquake are smaller (50 to 100 kPa; Fig. 4a). In a region south of the southern Hawkes Bay SSE, the plate interface is fully locked[37], and there were no observable SSEs following the earthquake despite large (>400 kPa) dynamic-stress changes (Fig. 4a). To demonstrate the role that the low-velocity sedimentary wedge of the outer forearc plays, we compare amplitude and duration results

with those from a 1D layered velocity model (Fig. 4 and Supplementary Fig. 9). The presence of the low-velocity sedimentary wedge above the shallow interface promotes larger and longer-lasting stress changes compared with the 1D case. The relative amplitude and pattern of static- and dynamic-stress changes do not depend significantly on the assumed effective coefficient of friction (Supplementary Fig. 8).

These results suggest that shallow subduction interfaces overlain by a low-velocity sedimentary wedge can be highly susceptible to dynamic triggering of slip events (aseismic or seismic) by regional earthquakes. Northward rupture directivity also plays a role in the amplitude of dynamic-stress changes on the shallow interface and is enhanced by interactions with the low-velocity sedimentary wedge sitting above the high-velocity subducted oceanic crust (Fig. 4 and Supplementary Fig. 9). The low-velocity wedge acts as a waveguide, trapping seismic energy[42] along the Hikurangi margin and promoting triggering of shallow SSEs by amplifying and increasing the duration of the dynamic stressing (Fig. 4a,d). The low-velocity outer forearc's impact on the duration of dynamic stressing is further illustrated by animations of seismic wave passage, comparing the 1D and 3D velocity model cases (Supplementary Movies). Amplification of dynamic stresses by the presence of an overlying sedimentary basin has also been suggested as a mechanism for dynamic triggering of the 2013 $M7.5$ Craig earthquake three months after the 2012 $M7.7$ Haida Gwaii earthquake[43]. Another possible example is aftershocks triggered on or near the shallow subduction interface in Sumatra, within 1–2 min after a 2012 $M_w7.2$ intraslab earthquake ∼150 km away[44]. Potential for dynamic triggering of SSEs on shallow subduction interfaces will be augmented by the fact that high fluid pressures (and concomitant low effective stress) may be present on shallow subduction interfaces due to disequilibrium compaction of rapidly subducted, fluid-rich sediments[45].

Many (if not most) subduction zone outer forearcs are characterized by low seismic velocities[46–48]. It is possible that dynamic triggering of shallow subduction SSEs may be a common occurrence, although there are currently few regions where such shallow subduction SSEs can be detected, due to offshore observational limitations. Our result also raises the implication that shallow subduction interface earthquakes, such as tsunami earthquakes, may be more easily triggered by dynamic-stress changes from regional and distant earthquakes. To clarify, this does not imply that this results in an overall higher seismic hazard at shallow (<10 km) subduction interfaces, we suggest only that they are more susceptible to long-range, large-scale triggering than deeper interfaces. Dynamic triggering of SSEs and, potentially, earthquakes on shallow subduction thrusts may be common, due to properties of the overriding plate in these environments that amplify dynamic stresses from passing seismic waves.

Methods

Methods, including statements of data availability and any associated accession codes and references, are available in the online version of this paper.

References

1. Dragert, H., Wang, K. & James, T. A silent slip event on the deeper Cascadia subduction interface. *Science* **292,** 1525–1528 (2001).
2. Beroza, G. C. & Ide, S. Slow earthquakes and nonvolcanic tremor. *Annu. Rev. Earth Planet. Sci.* **39,** 271–296 (2011).
3. Peng, Z. & Gomberg, J. An integrated perspective of the continuum between earthquakes and slow-slip phenomena. *Nat. Geosci.* **3,** 599–607 (2010).
4. Schwartz, S. Y. & Rokosky, J. M. Slow slip events and seismic tremor at circum-pacific subduction zones. *Rev. Geophys.* **45,** RG3004 (2007).
5. Kato, A. *et al*. Propagation of slow slip leading up to the 2011 M_w 9.0 Tohoku-Oki earthquake. *Science* **335,** 705–708 (2012).
6. Ito, Y. *et al*. Episodic slow slip events in the Japan subduction zone before the 2011 Tohoku-Oki earthquake. *Tectonophysics* **600,** 14–26 (2013).
7. Obara, K. & Kato, A. Connecting slow earthquakes to huge earthquakes. *Science* **353,** 253–257 (2016).
8. Radiguet, M. *et al*. Triggering of the 2014 M_w 7.3 Papanoa earthquake by a slow slip event in Guerrero, Mexico. *Nat. Geosci.* **9,** 829–834 (2016).
9. Ruiz, S. *et al*. Intense foreshocks and a slow slip event preceded the 2014 Iquique M_w 8.1 earthquake. *Science* **345,** 1165–1169 (2014).
10. Peng, Z. & Chao, K. Non-volcanic tremor beneath the Central Range in Taiwan triggered by the 2001 M_w7.8 Kunlun earthquake. *Geophys. J. Int.* **175,** 825–829 (2008).
11. Rubinstein, J. L. *et al*. Seismic wave triggering of nonvolcanic tremor, episodic tremor and slip, and earthquakes on Vancouver Island. *J. Geophys. Res.* **114,** B00A01 (2009).
12. Fry, B., Chao, K., Bannister, S., Peng, Z. & Wallace, L. Deep tremor in New Zealand triggered by the 2010 M_w8.8 Chile earthquake. *Geophys. Res. Lett.* **38,** L15306 (2011).
13. Francoiş-Holden, C. *et al*. The M_w 6.6 Gisborne Earthquake of 2007: preliminary records and general source characterisation. *Bull. NZ Soc. Earthq. Eng.* **41,** 266–277 (2008).
14. Hirose, H., Hirahara, K., Kimata, F., Fujii, N. & Miyazaki, S. A slow thrust slip event following the two 1996 Hyuganada Earthquakes beneath the Bungo Channel, southwest Japan. *Geophys. Res. Lett.* **26,** 3237–3240 (1999).
15. Itaba, S. & Ando, R. A slow slip event triggered by teleseismic surface waves. *Geophys. Res. Lett.* **38,** L21306 (2011).
16. Zigone, D. *et al*. Triggering of tremors and slow slip event in Guerrero, Mexico, by the 2010 M_w8.8 Maule, Chile, earthquake. *J. Geophys. Res.* **117,** http://dx.doi.org/10.1029/2012JB009160 (2012).
17. Araki, E. *et al*. Recurring and triggered slow slip events near the trench at the Nankai Trough subduction megathrust. *Science* **356,** 1157–1160 (2017).
18. Hirose, H., Kimura, H., Enescu, B. & Aoi, S. Recurrent slow slip event likely hastened by the 2011 Tohoku earthquake. *Proc. Natl Acad. Sci. USA* **109,** 15157–15161 (2012).
19. Wei, M., Liu, Y., Kaneko, Y., McGuire, J. & Bilham, R. Dynamic triggering of creep events in the Salton Trough, Southern California by regional M ≥ 5.4 earthquakes constrained by geodetic observations and numerical simulations. *Earth Planet. Sci. Lett.* **427,** 1–10 (2015).
20. Peng, Z., Shelly, D. R. & Ellsworth, W. L. Delayed dynamic triggering of deep tremor along the Parkfield-Cholame section of the San Andreas Fault following the 2014 M6.0 South Napa earthquake. *Geophys. Res. Lett.* **42,** 7916–7922 (2015).
21. Hamling, I. J. *et al*. Complex multi-fault rupture during the 2016 M_w 7.8 Kaikōura earthquake, New Zealand. *Science* **356,** 6334 (2017).
22. Kaiser, A. *et al*. The Kaikōura (New Zealand) earthquake: preliminary seismological report. *Seismol. Res. Lett.* **88,** 727–739 (2017).
23. Wallace, L. M. & Beavan, J. Diverse slow slip behavior at the Hikurangi subduction margin, New Zealand. *J. Geophys. Res.* **115,** B12402 (2010).
24. McCaffrey, R. Time-dependent inversion of three-component continuous GPS for steady and transient sources in northern Cascadia. *Geophys. Res. Lett.* **36,** GL036784 (2009).
25. Williams, C. A. *et al*. Revised interface geometry for the Hikurangi subduction zone, New Zealand. *Seismol. Res. Lett.* **84,** 1066–1073 (2013).
26. Segall, P. & Matthews, M. Time dependent inversion of geodetic data. *J. Geophys. Res.* **102,** 22391–22409 (1997).
27. Miyazaki, S., Segall, P., McGuire, J. J., Kato, T. & Hatanaka, Y. Spatial and temporal evolution of stress and slip rate during the 2000 Tokai slow earthquake. *J. Geophys. Res.* **111,** B03409 (2006).
28. Wallace, L. M., Beavan, J., Bannister, S. & Williams, C. Simultaneous long-term and short-term slow slip events at the Hikurangi subduction margin, New Zealand: implications for processes that control slow slip event occurrence, duration, and migration. *J. Geophys. Res.* **117,** B11402 (2012).
29. Bartlow, N. M., Wallace, L. M., Beavan, R. J., Bannister, S. & Segall, P. Time-dependent modeling of slow slip events and associated seismicity and tremor at the Hikurangi subduction zone, New Zealand. *J. Geophys. Res.* **119,** 734–753 (2014).
30. Ristau, J. Implementation of routine regional moment tensor analysis in New Zealand. *Seismol. Res. Lett.* **79,** 400–415 (2008).
31. Meng, L., Huang, H., Bürgmann, R., Ampuero, J. P. & Strader, A. Dual megathrust slip behaviors of the 2014 Iquique earthquake sequence. *Earth Planet. Sci. Lett.* **411,** 177–187 (2015).
32. Kodaira, S. *et al*. High pore fluid pressure may cause silent slip in the Nankai Trough. *Science* **304,** 1295–1298 (2004).
33. Liu, Y. & Rice, J. R. Spontaneous and triggered aseismic deformation transients in a subduction fault model. *J. Geophys. Res.* **112,** B09404 (2007).

34. Rubinstein, J. L., La Rocca, M., Vidale, J. E., Creager, K. C. & Wech, A. G. Tidal modulation of nonvolcanic tremor. *Science* **319,** 186–189 (2008).
35. Thomas, A., Nadeau, R. M. & Bürgmann, R. Tremor-tide correlations and near-lithostatic pore pressure on the deep San Andreas fault. *Nature* **462,** 1048–1051 (2009).
36. Hamling, I. J. *et al*. Stress transfer between thirteen successive dyke intrusions in Ethiopia. *Nat. Geosci.* **3,** 713–717 (2010).
37. Wallace, L. M. *et al*. The kinematics of a transition from subduction to strike-slip: an example from the central New Zealand plate boundary. *J. Geophys. Res.* **117,** B02405 (2012).
38. King, G. C., Stein, R. S. & Lin, J. Static stress changes and the triggering of earthquakes. *Bull. Seismol. Soc. Am.* **84,** 935–953 (1994).
39. Cochran, E., Vidale, J. & Tanaka, S. Earth tides can trigger shallow thrust fault earthquakes. *Science* **306,** 1164–1166 (2004).
40. van der Elst, N. J. & Brodsky, E. E. Connecting near-field and far-field earthquake triggering to dynamic strain. *J. Geophys. Res.* **115,** B07311 (2010).
41. Hill, D. P. & Prejean, S. in *Treatise on Geophysics* Vol. 4, 2nd edn (ed. Kanamori, H.) 273–304 (Elsevier, 2015).
42. Olsen, K. B. *et al*. Strong shaking in Los Angeles expected from southern San Andreas earthquake. *Geophys. Res. Lett.* **33,** L07305 (2006).
43. Gomberg, J. Permanently enhanced dynamic triggering probabilities as evidenced by two M>7.5 earthquakes. *Geophys. Res. Lett.* **40,** 4828–4833 (2013).
44. Fan, W. & Shearer, P. M. Fault interaction and triggering during the 10 January 2012 M_w 7.2 Sumatra earthquake. *Geophys. Res. Lett.* **43,** 1934–1942 (2016).
45. Saffer, D. M. & Wallace, L. M. The frictional, hydrologic, metamorphic, and thermal habitat of shallow slow earthquakes. *Nat. Geosci.* **8,** 594–600 (2015).
46. Kamei, R., Pratt, R. G. & Tsuji, T. Waveform tomography imaging of a megasplay fault system in the seismogenic Nankai subduction zone. *Earth Planet. Sci. Lett.* **317–318,** 343–353 (2012).
47. Bassett, D., Sutherland, R., and, S. & Henrys, S. Slow wavespeeds and fluid overpressure in a region of shallow geodetic locking and slow slip, Hikurangi subduction margin, New Zealand. *Earth Planet. Sci. Lett.* **389,** 1–13 (2014).
48. Bangs, N. L. B., Westbrook, G. K. & Ladd, J. W. Seismic velocities from the Barbados ridge complex: indicators of high pore fluid pressures in an accretionary complex. *J. Geophys. Res.* **95,** 8767–8782 (1990).

Author contributions

L.M.W. conceived the study, undertook the TDEFNODE inversions, and led the writing of the paper. Y.K. undertook the dynamic-stress-change modelling, and contributed to the interpretations and writing of the paper. N.B. was responsible for the Network Inversion Filter inversions. I.H. undertook the Coulomb stress change modelling. S.H. and E.D'A. undertook processing of the cGPS data. Z.P. and B.F. contributed locations of repeaters during the SSE and provided seismological expertise and insights into remote triggering of SSEs.

Additional information

Supplementary information is available in the online version of the paper. Reprints and permissions information is available online at www.nature.com/reprints. Publisher's note: Springer Nature remains neutral with regard to jurisdictional claims in published maps and institutional affiliations. Correspondence and requests for materials should be addressed to L.M.W.

Competing financial interests

The authors declare no competing financial interests.

Methods

GPS and seismological data used in this study are available from www.geonet.org.nz.

Inversions for SSE slip using TDEFNODE. SSE slip inversions in Figs 1 and 3 are undertaken with TDEFNODE[24] (http://web.pdx.edu/~mccaf/www/defnode/tdefnode.html), which is a nonlinear time-dependent inversion code that applies simulated annealing to downhill simplex minimization. We invert the cGPS time series of GeoNet sites in the North Island for: a time-constant describing the temporal evolution of two transient events describing the northern and central Hikurangi SSE slip; and the maximum amplitude of slip at 60 nodes on the interface offshore the central and northern Hikurangi margin. Slip on fault patches between the nodes is determined by bi-linear interpolation. TDEFNODE uses basis functions to describe the temporal evolution of slip at the nodes, thus reducing the number of free parameters required to replicate the temporal evolution of the SSE. We assume an exponential function to approximate the time history of slip in the northern half of the SSE, and a Gaussian function for the southern half of the SSE. Decisions on which functional forms to use for each transient were determined by trial and error—due to the immediate and rapid onset of the northern SSE region, an exponential function fitted the cGPS time series better for the northern Hikurangi portion of the SSE, while a slower rise time for the SSE at the central Hikurangi margin (southern Hawkes Bay) was better approximated by a Gaussian function. We assume slip on the plate interface occurs in the direction of plate motion slip determined by previous elastic block modelling results[37]; for the east coast, slip is almost completely in the down-dip direction. Fits to many of the time series are shown in Supplementary Fig. 4a (24-h solutions) and Supplementary Fig. 4b (8-h solutions).

Inversions for SSE slip using the Network Inversion Filter. We use the Network Inversion Filter[26,27] (NIF) to create a time-dependent model of slip and slip rate on the plate interface for the period 14 November 2016 to 1 January 2017 (see Supplementary Fig. 2). At each time t, this Kalman-filter-based method models a vector of station positions $\mathbf{d}(t)$ as a sum of a vector of initial positions ($\mathbf{d}(t_0)$); the product of a matrix of Green's function multipliers that map slip on each triangular subfault to displacement at each station ($\mathbf{G}$) and the slip on each subfault since the initial time t_0 ($\mathbf{s}(t - t_0)$); the product of a matrix representing a shift of the entire network ($\mathbf{F}$) and time-varying reference frame errors ($\mathbf{f}(t)$); the random walk errors as a function of time ($\mathbf{l}(t - t_0)$); and white noise ($\boldsymbol{\epsilon}$) (equation (1)).

$$\mathbf{d}(t) = \mathbf{d}(t_0) + \mathbf{Gs}(t - t_0) + \mathbf{Ff}(t) + \mathbf{l}(t - t_0) + \boldsymbol{\epsilon} \qquad (1)$$

The NIF first steps forward and then steps backward through the data, creating a model at each time step that is dependent on all past and future data. The power of the NIF lies in its ability to simultaneously model all data from all stations, allowing better discrimination of signal versus noise. The NIF implements both temporal and spatial smoothing hyperparameters, referred to as α and γ respectively. Temporal smoothing is implemented in the process noise matrix[26], and Laplacian spatial smoothing is implemented via a pseudo observation method[27]. Temporal smoothing is performed both forwards and backwards in time. This creates a more stable model but allows changes in slip rate that appear in the model before displacement rates change at the GPS stations, typically by a few days[49]. This is the most likely explanation for why slip in the southern Hawkes Bay region appears earlier and lasts longer in the NIF-based model as compared with the TDEFNODE inversion results (Fig. 3 and Supplementary Fig. 2). The smoothing parameters are chosen to be the same as those in a previous large-scale NIF-based study of SSEs in Hikurangi[29], and uncertainties in the model are also discussed there. A weak non-negativity constraint is imposed on slip rate[50].

GPS data processing. The 24-h solutions used in the time-dependent inversions are provided by GeoNet, and more details on the processing used for these can be found at http://www.geonet.org.nz/data/supplementary/gnss_time_series_notes. For the 8-h solutions (Fig. 2, right panels), the data were analysed using the GAMIT/GLOBK software, version 10.6. The New Zealand cGPS data were divided into 8-h sessions for better temporal resolution but using a 24-h running window of reference station and orbit data in the analysis. We solve for station coordinates in the ITRF14 reference frame, satellite orbit and Earth rotation parameters, atmospheric zenith delay every 2 h, and three atmospheric gradients per day. The IGS14 azimuth- and elevation-dependent absolute phase centre offsets were applied to all antennas and ocean loading was corrected for using the FES2004 model.

Calculation of dynamic-stress change. Dynamic-stress changes on the Hikurangi subduction interface induced by the $M7.8$ Kaikōura earthquake waves are computed using the open-source seismic wave propagation software SPECFEM3D[50,51]. Our approach incorporates the latest 3D velocity and attenuation models for the North Island of New Zealand[52,53] (Supplementary Fig. 7). To compute dynamic-stress changes, a kinematic source model of the Kaikōura earthquake is needed. Here the Kaikōura earthquake is approximated as a finite fault represented by 3,122 point sources with a Gaussian source-time function with

the half duration of 2.5 s. We use a geodetically derived slip model[21] as a constraint for the fault geometry and the final slip distribution, and vary only the rupture initiation times of fault segments associated with the Kaikōura earthquake (Supplementary Fig. 5). The rupture initiation times are calibrated by comparing synthetic velocity waveforms to 21 near-field strong-motion and high-rate GPS waveforms filtered between 3 and 60 s. We then use the best-fit source model and compute time-dependent stress perturbations filtered at a period of 3 s and longer, which are resolved into normal and shear stresses on the subduction interface. Near the source (<50 km from the rupture region), equivalent static-stress changes—the difference between the initial and final stress changes—are in good agreement (<10%) with those derived from a method that assumes a homogeneous elastic half-space (Fig. 4b). Numerical simulations are run on New Zealand's NeSI supercomputing cluster.

To assess the accuracy of dynamic-stress changes, which are approximately proportional to the amplitude of velocity seismograms, we compare the magnitude of three-component velocity seismograms $|\mathbf{v}|$ filtered between 3 and 60 s to observed ones at strong-motion stations across New Zealand (Supplementary Fig. 6). To minimize the site effects, stations classified as either 'hard rock', 'rock' or 'shallow soil' sites[54] are used for the comparison. The maximum amplitudes of $|\mathbf{v}|$ in the model agree well with the data (Supplementary Fig. 6). The histogram of the errors between computed and observed maximum amplitude of $|\mathbf{v}|$, error $=$ $(\max(|v|^{\mathrm{synthetics}}) - \max(|v|^{\mathrm{data}}))/\max(|v|^{\mathrm{data}}))$, is approximately log-normally distributed with the standard error of 34% (Supplementary Fig. 6). This means that the standard error in dynamic-stress changes is probably on a similar order. Some stations near the east coast of the North Island show surface ground motion lasting longer than 150 s that is not captured by the synthetic waveform (Supplementary Fig. 6), indicating that the actual seismic velocity in the low-velocity sedimentary wedge is even smaller than the current 3D model (Supplementary Fig. 7).

To quantify the amplification of dynamic stresses on the plate interface due to a low-velocity sedimentary wedge, we computed equivalent stress changes using a 1D, layered velocity model. The 1D velocity model was derived from the spatial average of seismic velocities (V_p and V_s), densities and anelastic attenuations (Q_p and Q_s) at difference depth slices within the North Island that excludes the offshore, low-velocity region (Supplementary Fig. 7). The peak amplitude and duration of positive dynamic stresses >50 kPa are compared in Fig. 4 and Supplementary Fig. 9. Both the peak amplitude and duration of large stress changes in the SSE source region are larger in the simulation with the 3D velocity model than the 1D layered model, suggesting that the triggering of the SSEs was enhanced by the basin effect combined with rupture directivity.

Detection of repeating earthquakes. Repeating earthquakes in this region are detected on the basis of waveform cross-correlations of 17,962 events within the rectangular region (longitude: 175.5° E–177.5° E; latitude: −41° S–40° S) from 1 January 2010 to 10 January 2017. The method generally follows that used previously[31,55] and is briefly described here. We first download the event-based waveforms from the GEONET. Then we apply a 2–16 Hz bandpass filter to the vertical-component data, and compute cross-correlation (CC) values for all 56 stations with a minimum number of 1,000 events. We use 0.5 s before and 15.5 s after (total 16 s window) the network picked P-wave arrivals for computing the CC values with a maximum time lag of 4 s. Next, we select as a potential repeating event pair when at least two stations have CC values greater than 0.95. The resulting repeating pairs are grouped into repeating clusters using an equivalency class algorithm[55,56]. Supplementary Fig. 10 shows the waveform example of cluster C1369 recorded at station PRHZ. Out of 17,962 events, we detect a total of 1,398 repeating clusters (with at least two members in each cluster), and the total number of repeating events is 4,082 (~23%). Most repeating earthquakes occurred in the aftershock zone of the 20 January 2014 $M6.23$ Eketahuna earthquake (Supplementary Fig. 9). However, we also observe many repeating clusters near or off the coast of southern Hawkes Bay. Their occurrence was probably associated with the shallow SSE (Fig. 3).

Data availability. All GPS and seismological data used in this study are available at www.geonet.org.nz.

References

49. Bartlow, N. M., Miyazaki, S., Bradley, A. M. & Segall, P. Space-time correlation of slip and tremor during the 2009 Cascadia slow slip event. *Geophys. Res. Lett.* **38,** L18309 (2011).
50. Komatitsch, D. & Tromp, J. Introduction to the spectral elemental method for three-dimensional seismic wave propagation. *Geophys. J. Int.* **139,** 806–822 (1999).
51. Komatitsch, D. & Vilotte, J.-P. The spectral element method: an efficient tool to simulate the seismic response of 2D and 3D geological structures. *Bull. Seismol. Soc. Am.* **88,** 368–392 (1998).
52. Eberhart-Phillips, D., Reyners, M., Bannister, S., Chadwick, M. & Ellis, S. Establishing a versatile 3-D seismic velocity model for New Zealand. *Seismol. Res. Lett.* **81,** 992–1000 (2010).

53. Eberhart-Phillips, D. & Banninster, S. 3-D imaging of the northern Hikurangi subduction zone, New Zealand: variations in subducted sediment, slab fluids, and slow slip. *Geophys. J. Int.* **201,** 838–855 (2015).

54. Kaiser, A., Van Houtte, C., Perrin, N., Wotherspoon, L. & McVerry, G. Site characterisation of GeoNet stations for the New Zealand strong motion database. *Bull. NZ Soc. Earthq. Eng.* **50,** 39–49 (2017).

55. Peng, Z. & Ben-Zion, Y. Spatio-temporal variations of crustal anisotropy from similar events in aftershocks of the 1999 M7.4 İzmit and M7.1 Düzce, Turkey, earthquake sequences. *Geophys. J. Int.* **160,** 1027–1043 (2005).

56. Press, W. H. *FORTRAN Numerical Recipes: Numerical Recipes in FORTRAN 90* (Cambridge Univ. Press, 1996).

Large-scale dynamic triggering of shallow slow slip enhanced by overlying sedimentary wedge

Laura M. Wallace, Yoshihiro Kaneko, Sigrún Hreinsdóttir, Ian Hamling, Zhigang Peng, Noel Bartlow, Elisabetta D'Anastasio and Bill Fry

Figure S1: Displacement at North Island continuous GPS sites during the Kaikoura M7.8 earthquake determined by differencing the site positions for 5 days prior to the earthquake from the 12 hour period following the earthquake[20]. Since this represents displacements that include the twelve hours following the earthquake, some sites on the northeast coast also show eastward displacements from the SSE that initiated immediately following the earthquake (GISB, MAKO, CNST, MAHI; see also Fig. 2 in the main text). Coseismic displacement from the Kaikoura M7.8 earthquake at northern and central Hikurangi margin sites are small, generally 1-4 mm in the northward direction.
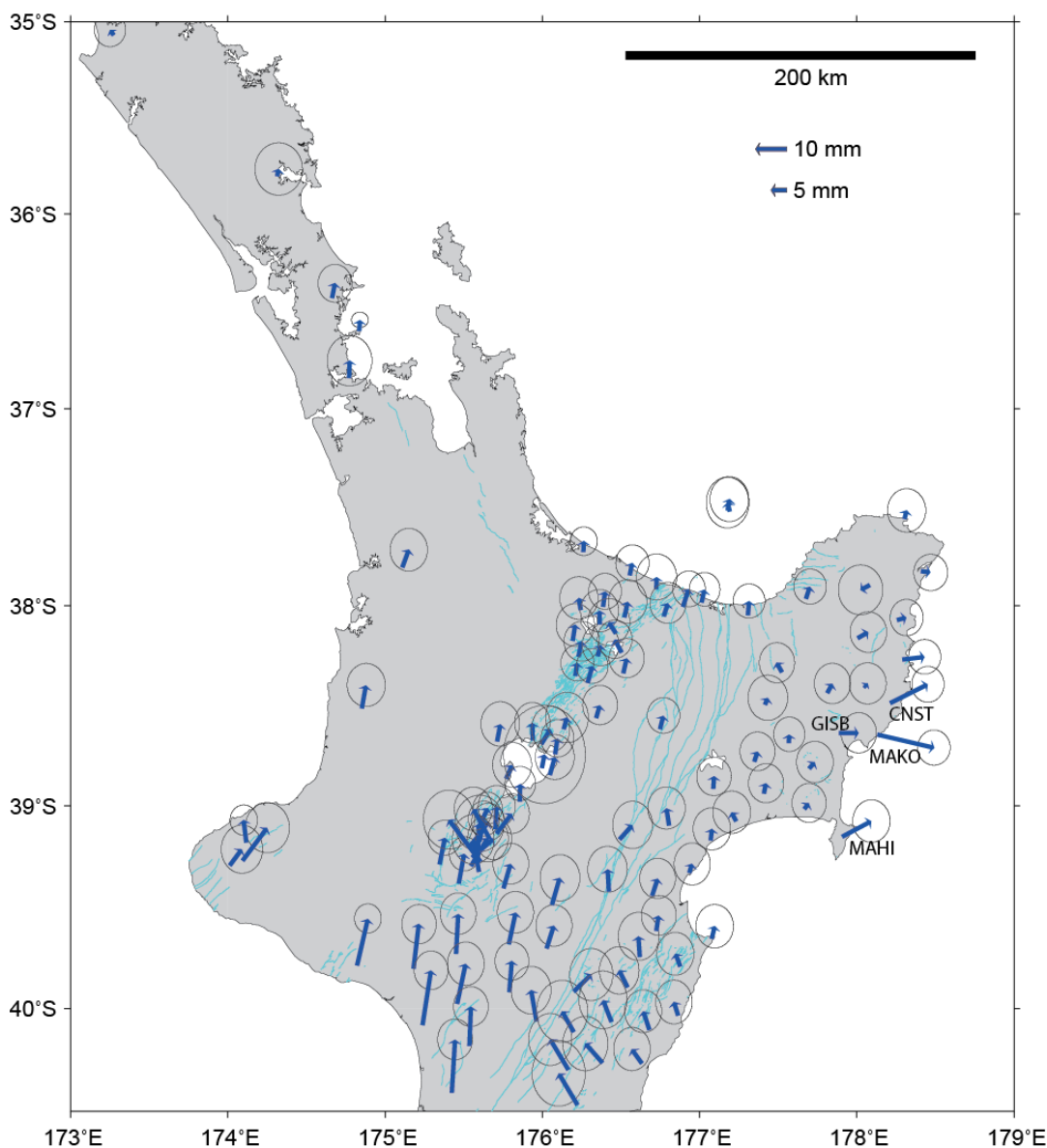
Figure S2: Results of SSE slip evolution using the Network Inversion Filter (NIF), using same timeframes as Figure 3 in the main text. There is excellent agreement between the NIF and TDefnode results, in terms of both the SSE evolution and slip magnitudes (compare with Fig. 3) Note the slightly earlier onset of the southern Hawkes Bay SSE and slightly later termination of the SSE in the NIF results (1-2 days) is likely a consequence of the temporal smoothing imposed in the NIF inversions.
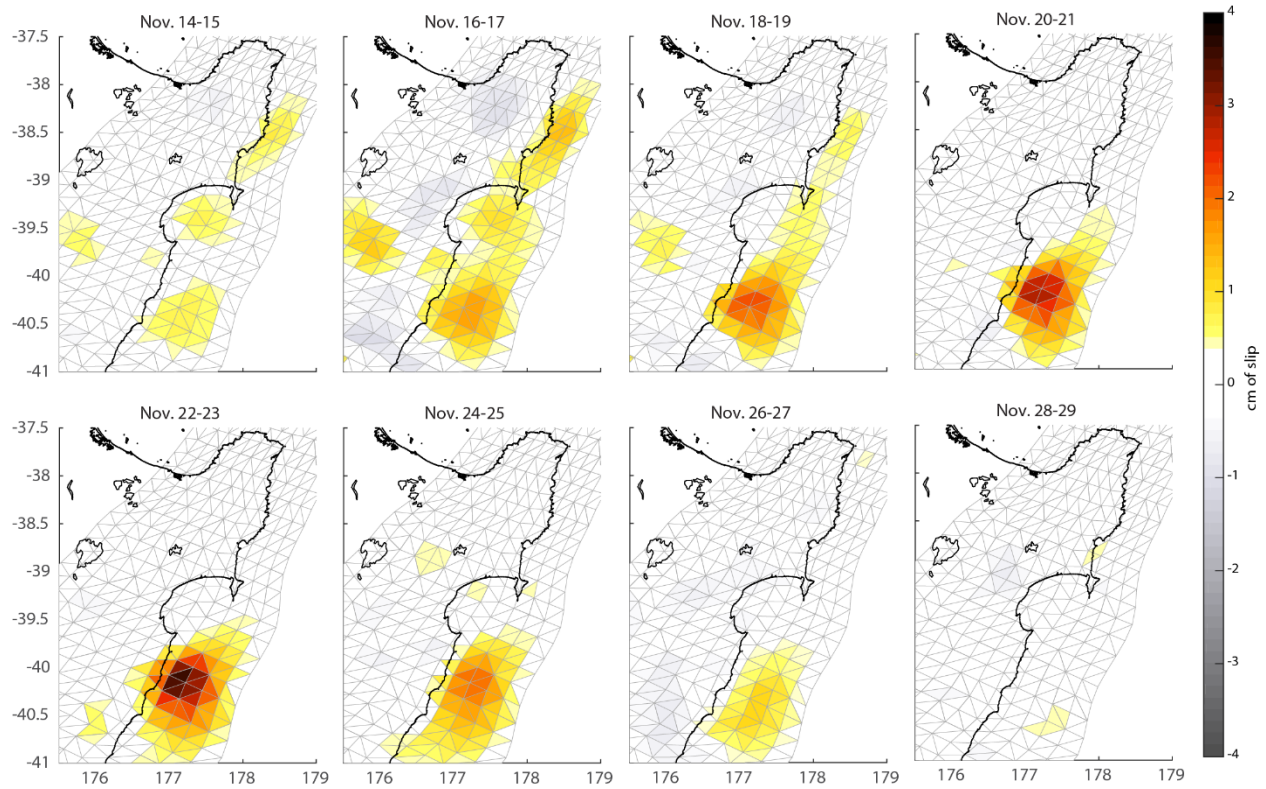
Figure S3: Timeseries of some representative cGPS sites (CNST, MAKO) on the coast of the northern Hikurangi margin for the year preceding the Kaikoura M7.8 earthquake to show that some SSEs had occurred in this region in the months prior to the larger SSE being triggered by the M7.8.
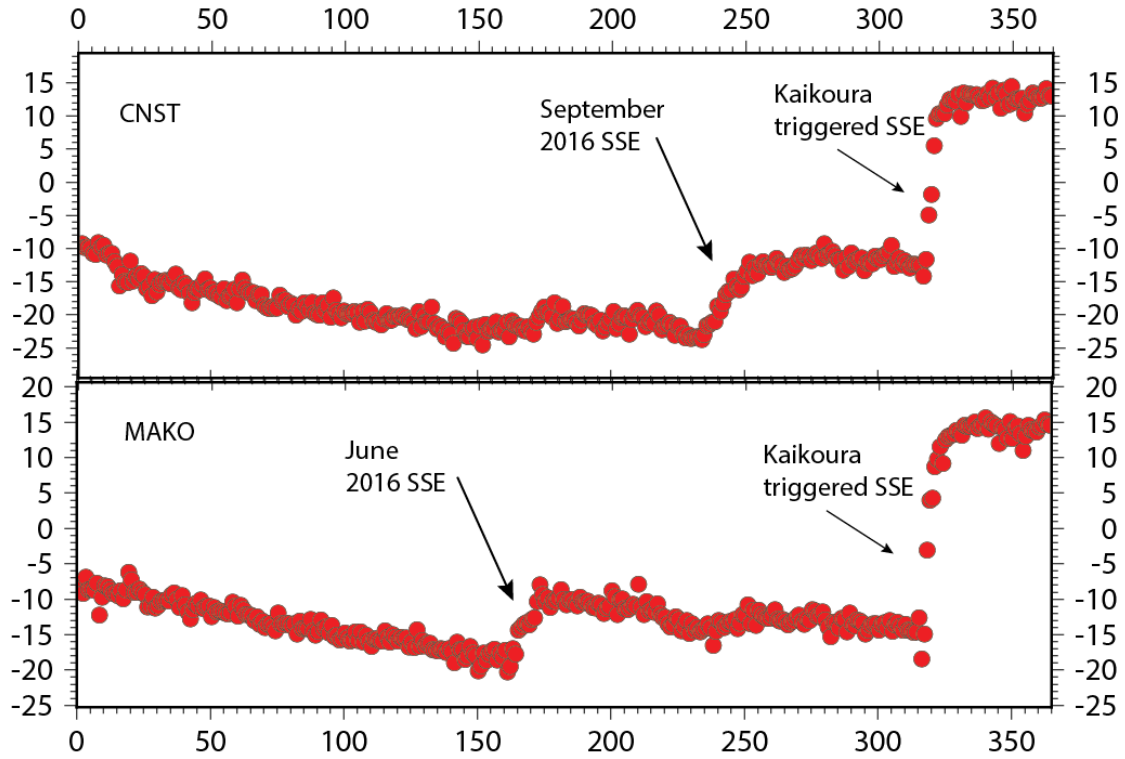
Figure S4(a): Timeseries of representative cGPS sites (east, north, and up components) impacted by the east coast SSE during the period following the Kaikoura M7.8 earthquake (circles for each daily position). The first day of the timeseries shown starts with the day after the Kaikoura earthquake. The black line shows the model fit to the timeseries from the TDefnode time-dependent inversions shown in Figures 1 and 3.
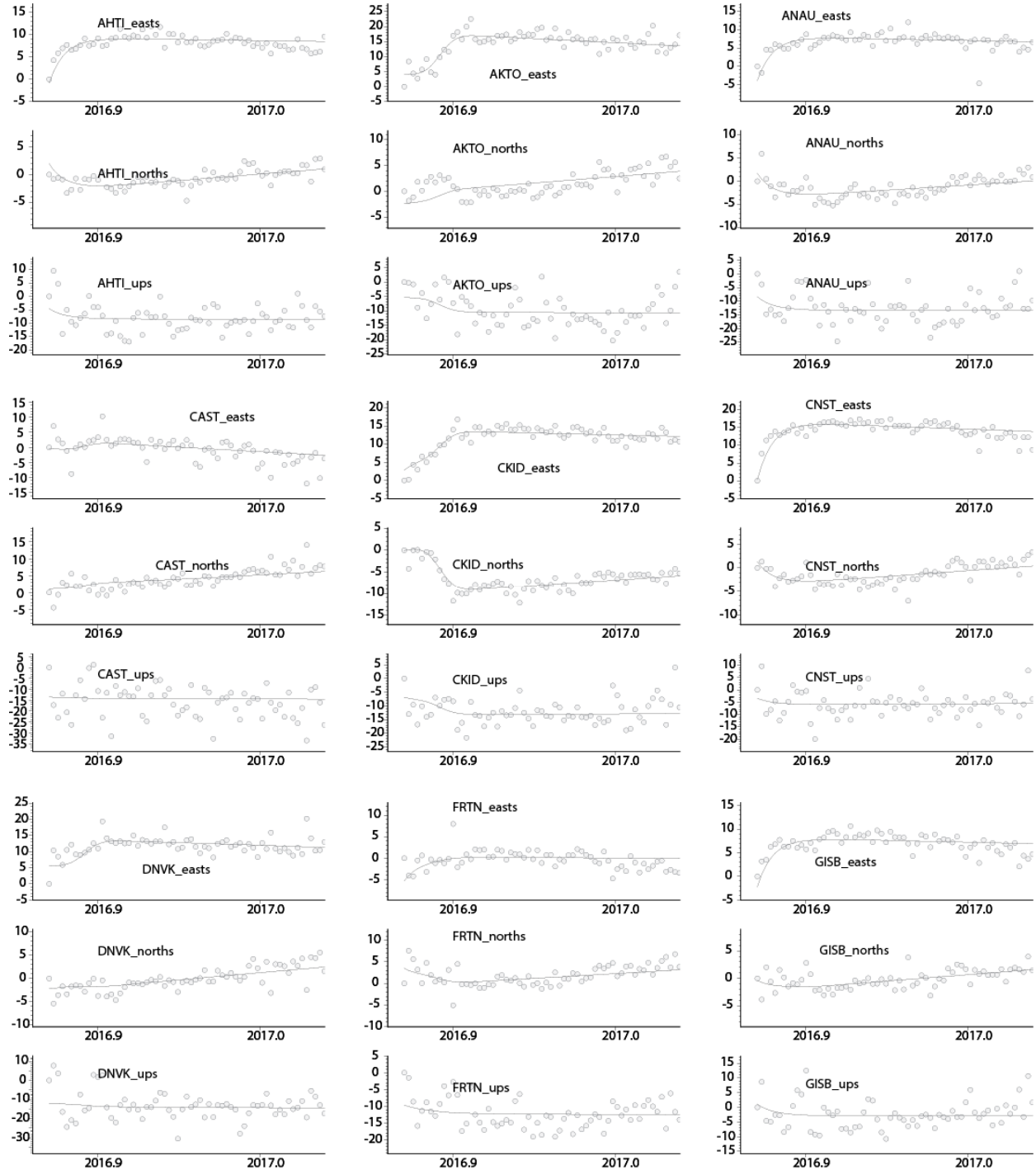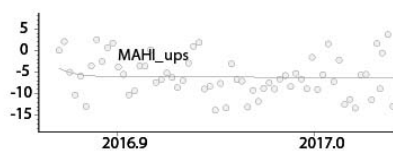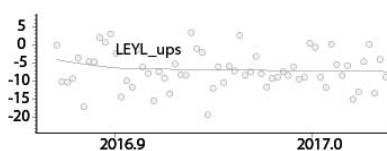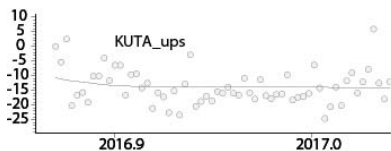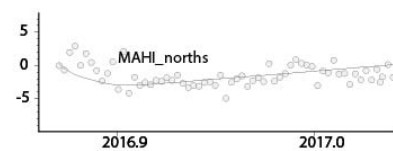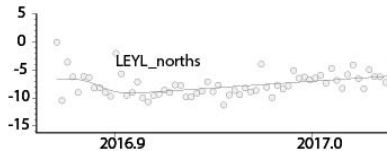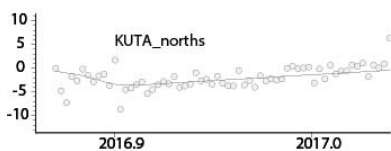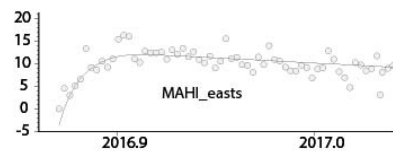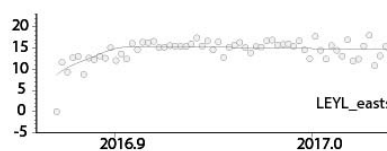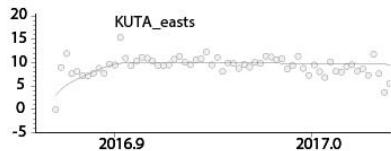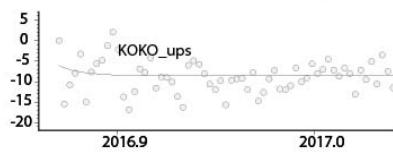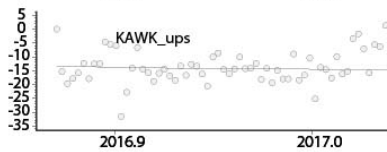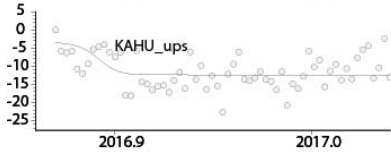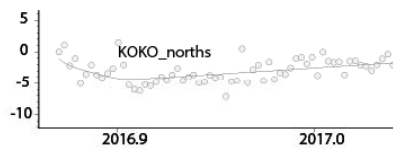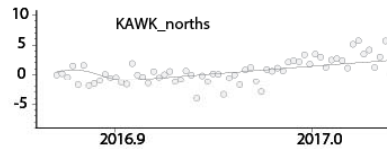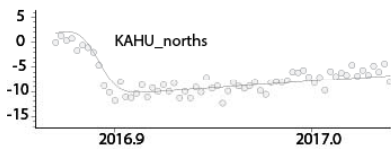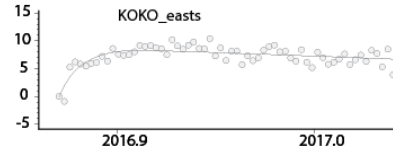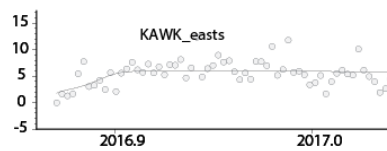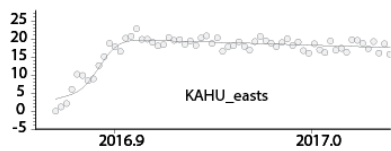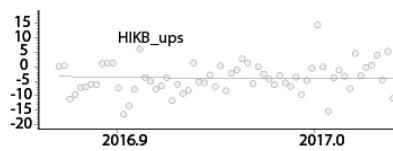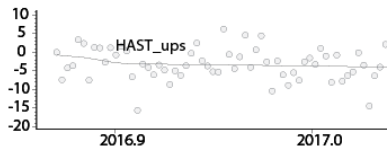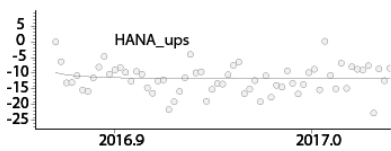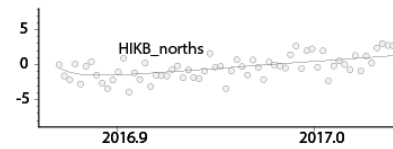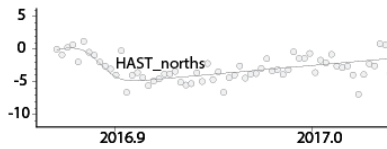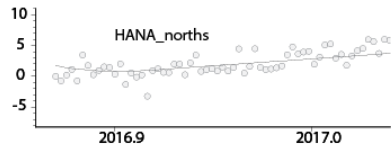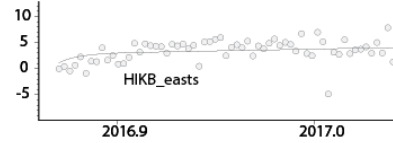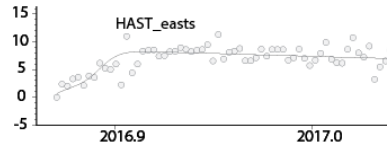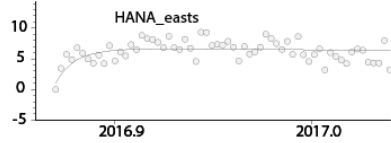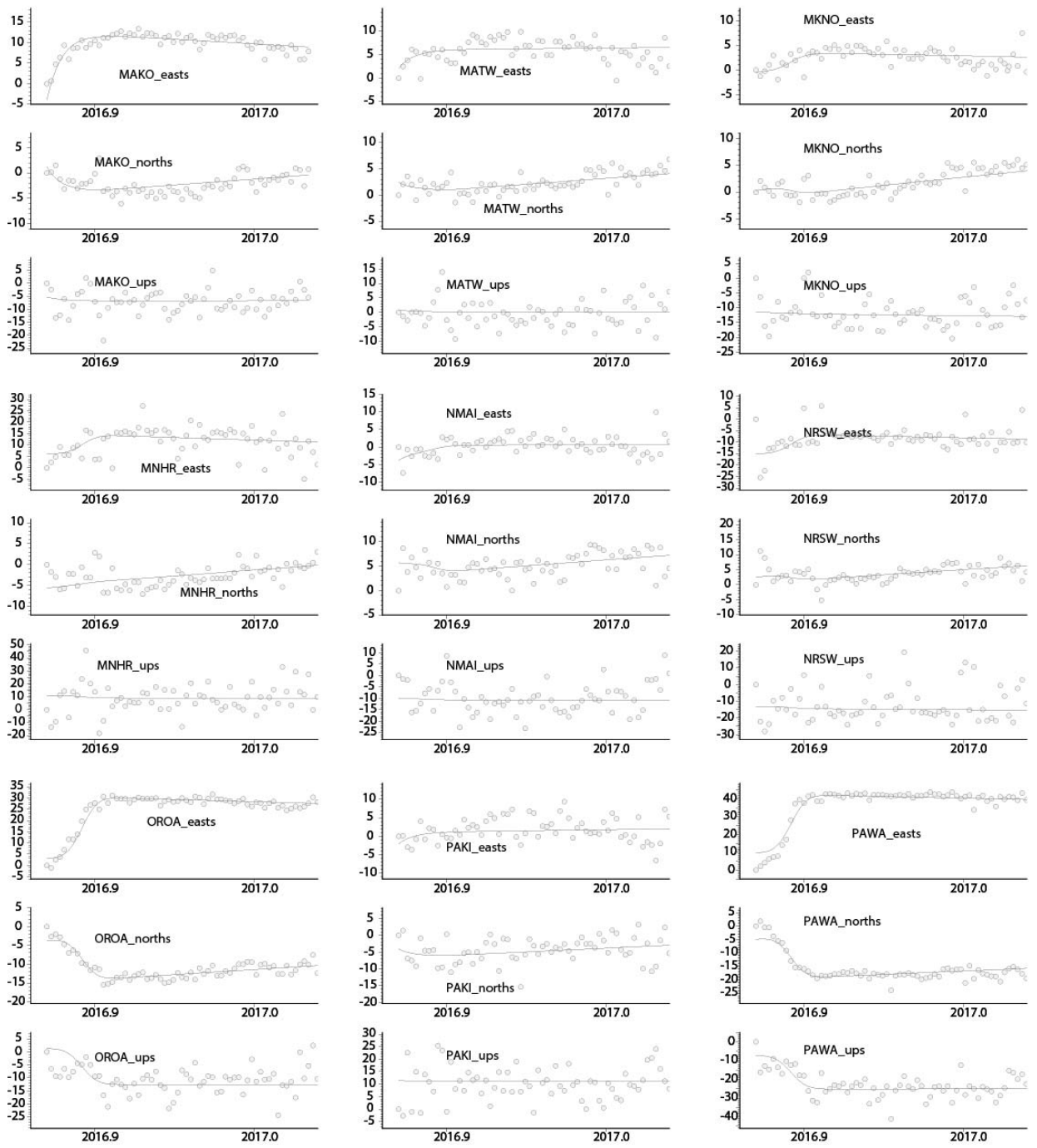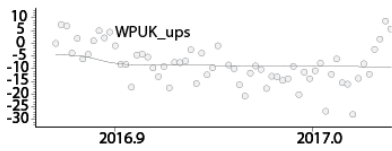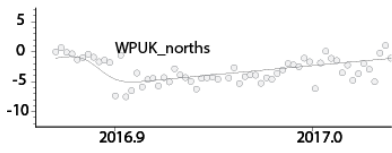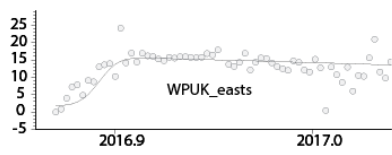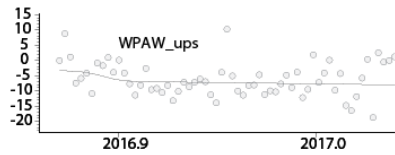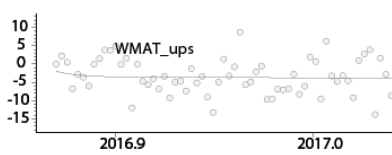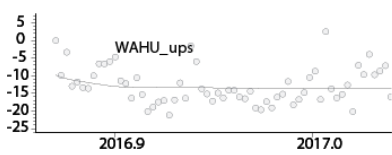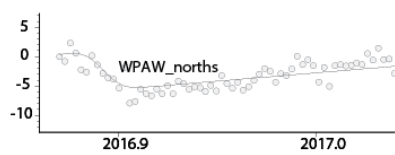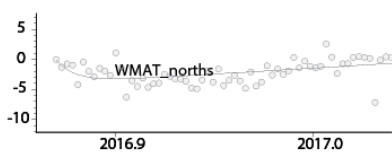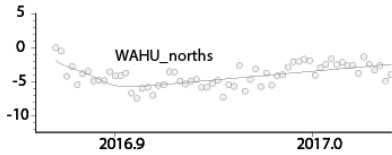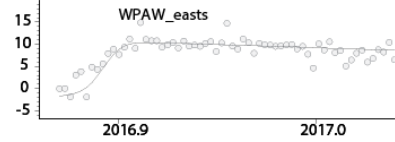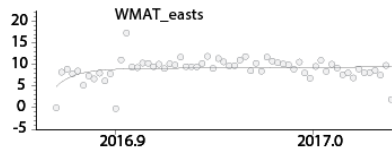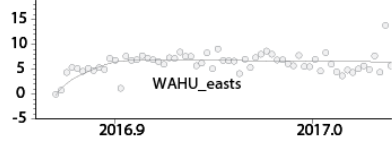
Figure S4(b): Timeseries of 8 hour solutions (e.g., Fig. 2b) for a subset of the cGPS sites (east and north components) impacted by the east coast SSE during the period following the Kaikoura M7.8 earthquake (circles for each 8 hour position). The first point of the timeseries shown starts two days before the Kaikoura earthquake. The black line shows the model fit to the timeseries from the TDefnode time-dependent inversions.
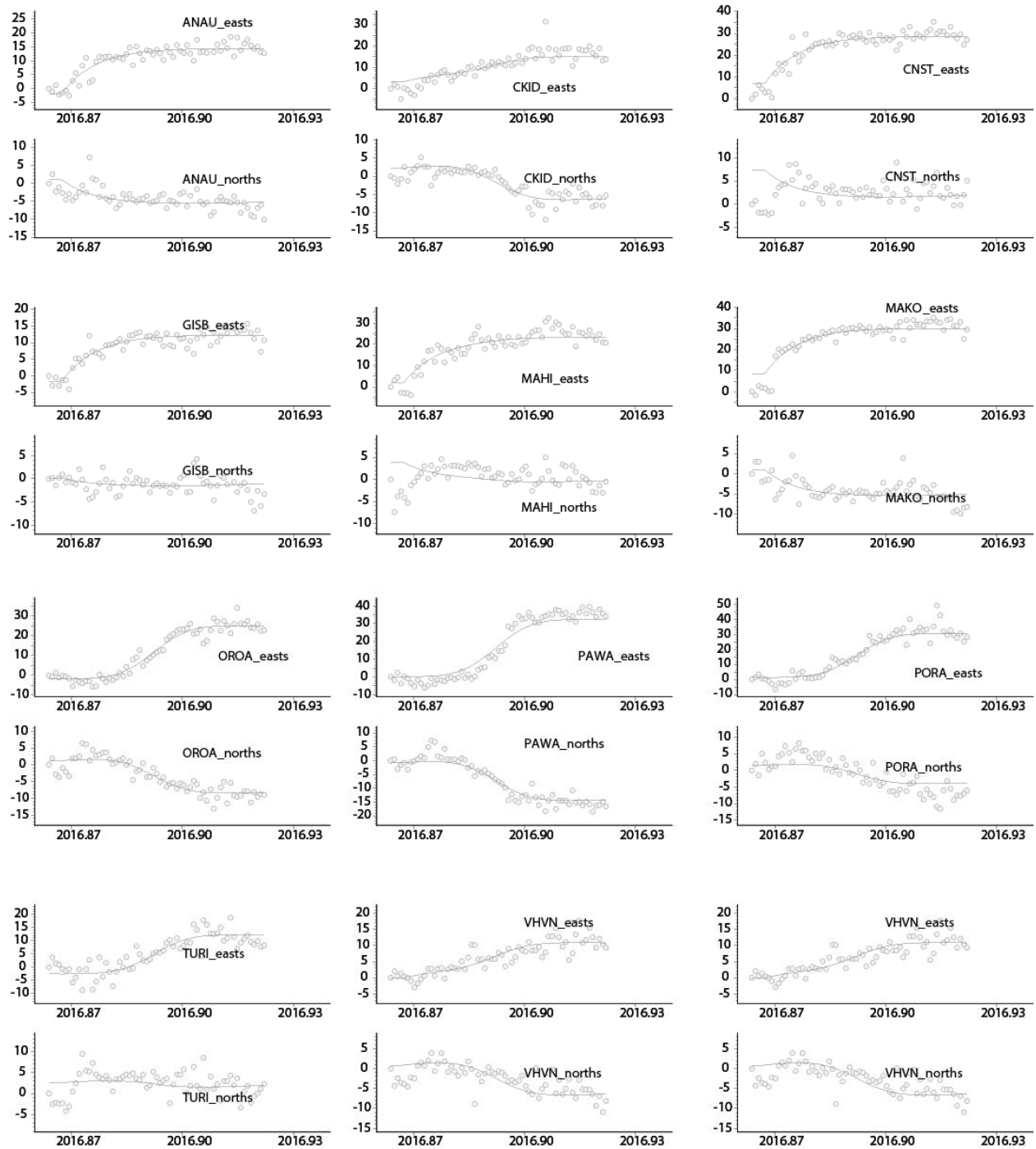
Figure S5: Kinematic source model of the M7.8 Kaikoura earthquake. Slip distribution associated with (A) the first rupture and (B) the secondary rupture. (C-D) The corresponding rupture time distributions. Star indicates the epicenter of the Kaikoura earthquake and triangles show the strong-motion and high-rate GPS stations used for calibrating the rupture times. The total slip from the first and second ruptures is equal to that in the geodetically-derived model[20]. The kinematic model indicates that the secondary rupture initiated at ~10 km depth in the southern Kekerengu fault at 59 seconds after the origin time and broke a major asperity with slip ~ 20 m in the deeper segment of the Kekerengu fault. Since assessing the accuracy of the kinematic source model is beyond the scope of this study, we validate the resulting ground velocity at strong motion stations across New Zealand as described in the text.
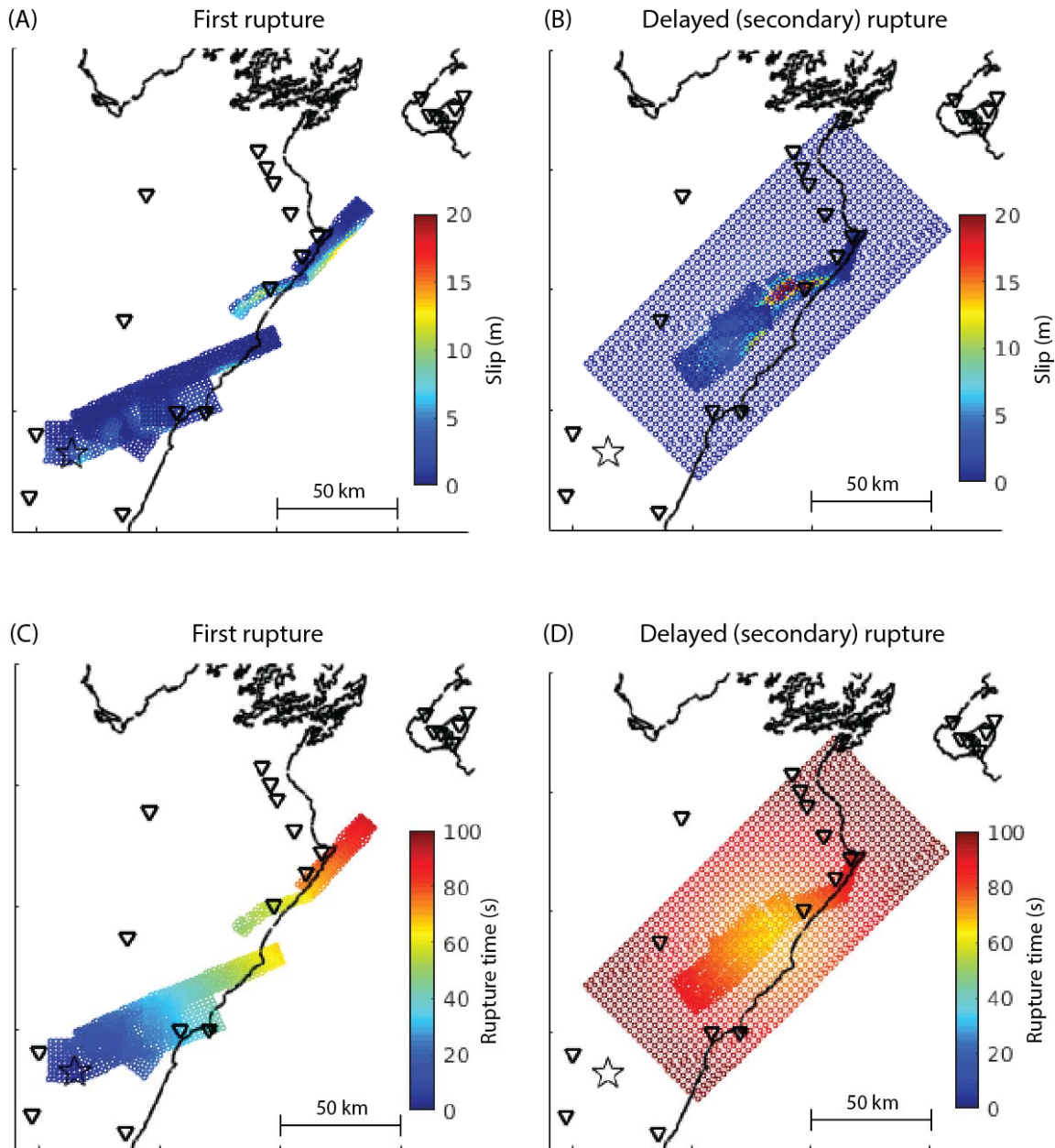
Figure S6: (A) A map of strong-motion stations used to compare observed and computed velocity waveforms. Star indicates the epicenter of the M7.8 Kaikoura earthquake. (B-F) Observed (black) and modeled (red) magnitude of three-component velocity waveforms |**v**| at selected stations. Waveforms recorded in the east coast of the North Island (e.g., GKBS) show amplified and long-lasting surface ground motions due to off-shore low-velocity sediments (Figure S7). (G) Comparison of observed and modeled maximum |**v**| at all the stations shown in the map. (F) Histogram of percentage errors of the maximum |**v**| between observed and modeled waveforms. The standard error is indicated.
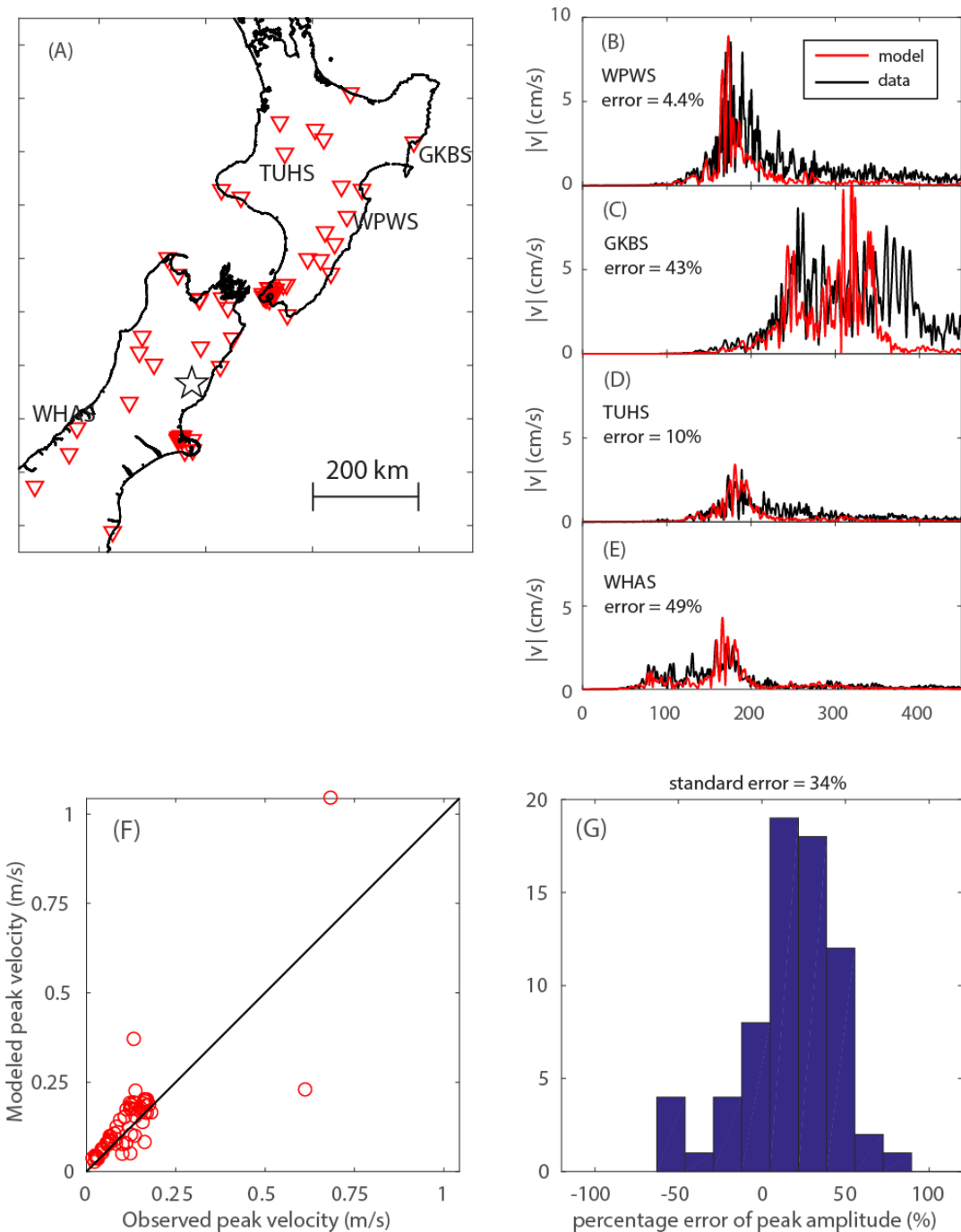
Figure S7: Map of shear-wave velocity at 3-km and 8-km depths[52,53] in the model. The offshore velocity is constrained by onshore-offshore data from marine air-gun shots recorded at onshore stations[52]. White dashed lines indicate the approximate boundary of good resolution in the model[52]. In off-shore regions south of Hawkes Bay, the model does not have good resolution due to lack of offshore data that were incorporated into the present model[53].
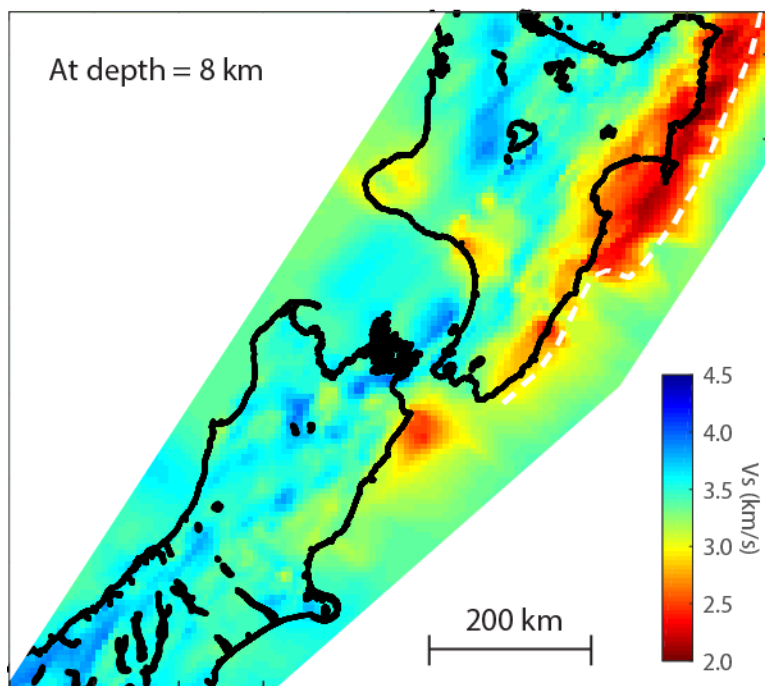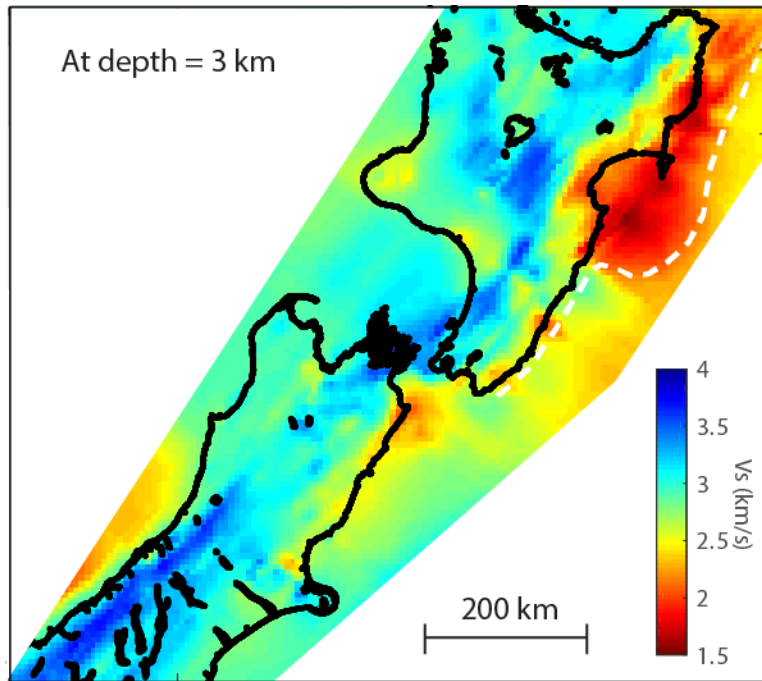
Figure S8: (a) Dynamic and (b) static stress changes induced by the M7.8 Kaikoura earthquake on the Hikurangi subduction interface assuming the effective coefficient of friction = 1.0.
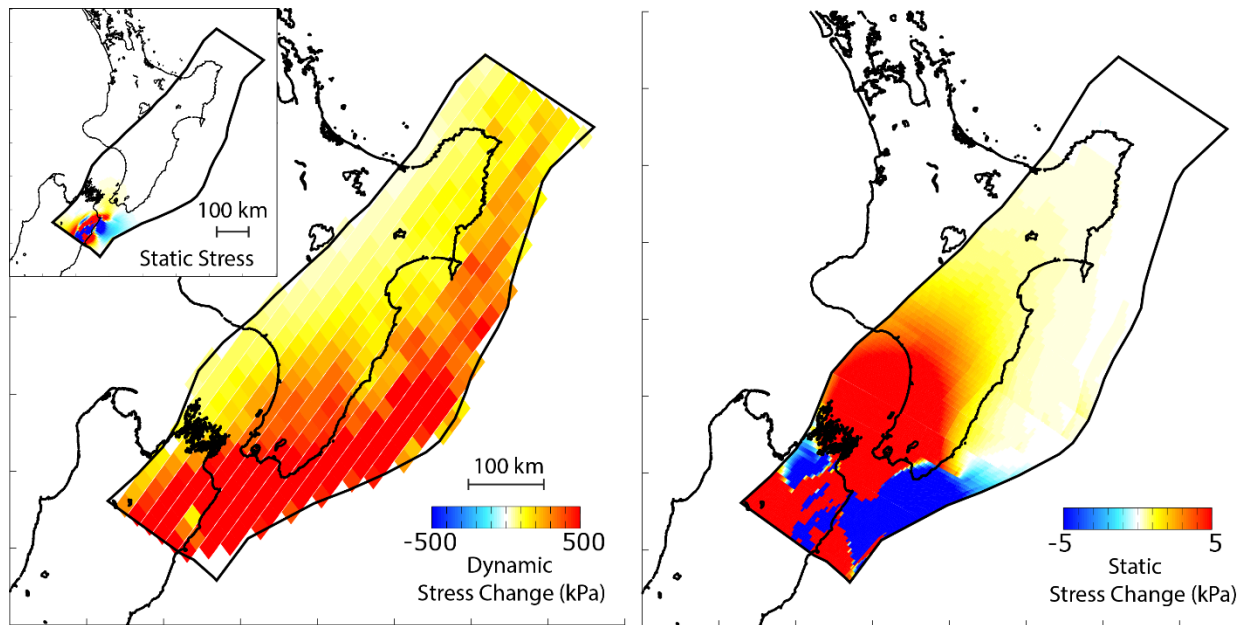
Figure S9: Total duration of dynamic stress changes larger than 50 kPa in (a) 3D and (b) 1D velocity models, induced by the M7.8 Kaikoura earthquake on the Hikurangi subduction interface assuming the effective coefficient of friction = 0.1. (c – f) Comparison of time histories of dynamic stress changes at selected locations in 3D and 1D velocity models.
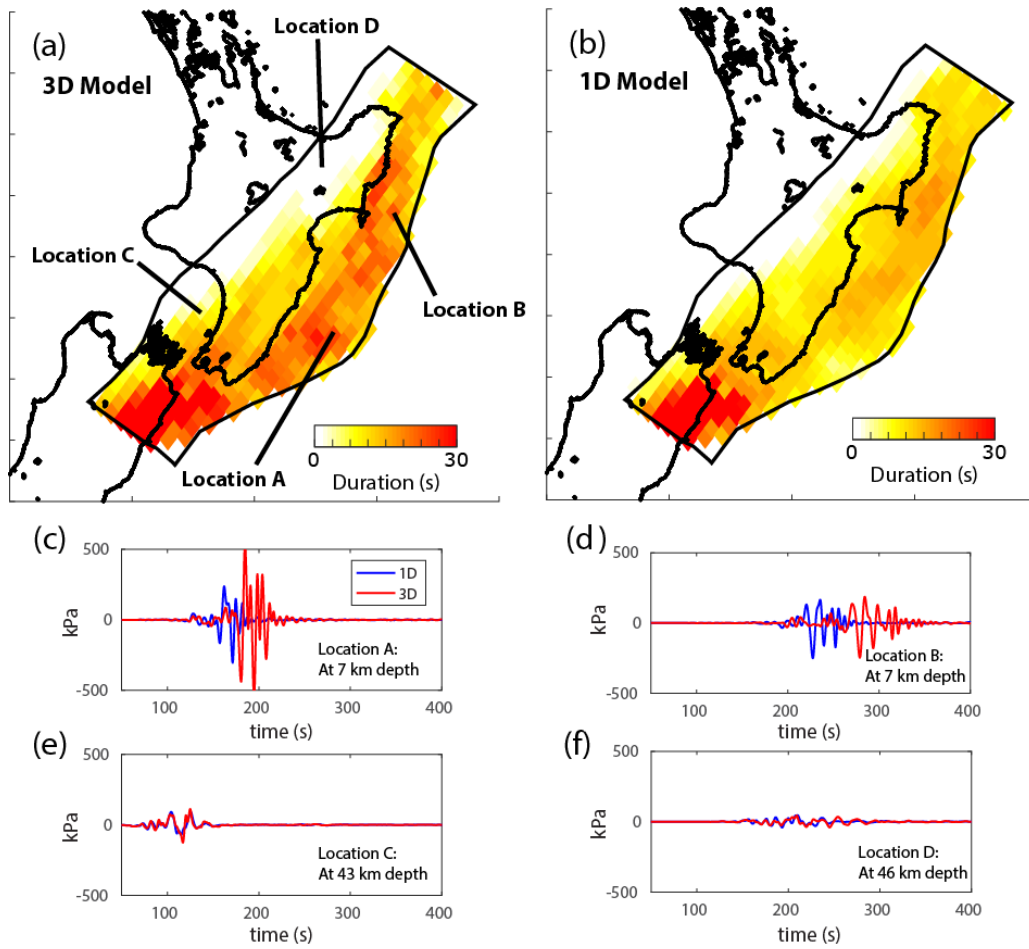
Figure S10: (a) A map showing the background seismicity from 2011-2016, repeating clusters with at least two (blue), five (green) and ten (red) events in each cluster. The white stars mark three earthquakes with magnitudes larger than 5.5, and the white circle marks the average location for cluster C1369. (b) 2-8 Hz band-pass-filtered vertical-component seismogram recorded at station PRHZ (for cluster C1369). The event origin time and magnitudes are marked to the right side of each trace.